PAPER • OPEN ACCESS

Pore-level CFD investigation of velocity and pressure dispositions in microcellular structures

View the article online for updates and enhancements.

Materials Research Express

PAPER

Pore-level CFD investigation of velocity and pressure dispositions in microcellular structures

A J Otaru [ORCID] **and M B Samuel**

Department of Chemical Engineering, Federal University of Technology, P.M.B. 065, Gidan-Kwanu Campus, Bida Road, Minna, Niger State, Nigeria

E-mail: otaru_12257@yahoo.com

Abstract

Pore-level computational modelling and simulation have recently become the focus of considerable attention in the field of transport in porous media. This study presents pore-structure characterisation and computational fluid dynamics (CFD) modelling and simulation of fluid flow distribution across 'real' and 'structure-adapted' porous metallic structures derived from tomography datasets at the microscale level. The resulting CFD predicted pressure drop data as a function of superficial fluid velocity ranging between 0 and 6.0 m.s^{-1} were used to account for the viscous (permeability, k_0) and inertial (Form drag coefficient, C) terms of the porous samples. CFD modelling confidence was established by validating with experimental measurements for foam samples available in the literature. Exprerimental values of k_0 were found to be consistent with values available in the literature, while observable deviations of experimental measurements of C from predicted values (in some cases) strongly support the reliability of the inertial terms in superficial fluid flow velocity, nature of fluid, and level of extended tortuous pathway in porous metallic structures. The adaptation of the 'real' structures through erosion and dilation of their skeletal phases enabled the creation of 'semi-virtual' structures; thereby providing an in-depth understanding of the manifestation of flowing fluid from Darcy to inertial and a graphical relationship linking pore-structure related parameters and fluid flow properties of the porous media was substantiated.

1. Background

Porous metallic structures are widely used as materials that interact with fluids, heat, pressure waves, and mechanical impact applications. Their unique and combined characteristics of high pore volume, high surface area, and high young modulus enables their suitability as a load-bearing structure for various engineering and industrial applications. Typical areas of applications for these materials are carbon dioxide capture and energy storage, filtration and waste reduction, sound absorption, biomedical devices, energy (oil and gas), and metallurgical processing, to name but a few. They are useful materials for the design of heat exchangers and acoustic absorbers. In the cement processing industries, porous metals are used as a medium for heat exchange between cooled air and cement clinker emitting from a cement kiln. In the oil and gas industries, porous metallic filters (PMF) are positioned as next generation screen materials for heavy oil and sand steam-assisted gravity (SAGD) applications for optimization of well performance for producing heavy crude oil and bitumen.

Porous metallic structures are categorised into open-celled and close-celled structures largely aided by their manufacturing routes and control of technological operating conditions [1–5]. The open-celled cellular materials (figure 1(a)) are characterised by an obvious and visible pore-network, variable cell size, pore-openings and a high 'air-filled' pore-volume fraction usually in the range of 0.75%–0.95% [6–8]. Close-celled cellular structures are characterised by low porosity ranging between 55 and 66%. Typical examples of close-celled structures are those made by replication casting processes of infiltrating liquid metals (at a high differential pressure, i.e. >1bar [figure 1(b)]) into the convergent gaps created by packed beds of porogens [9–17] and those formed by mechanical compaction of highly-porous open-celled structures [4, 18–23]. Studies have shown that
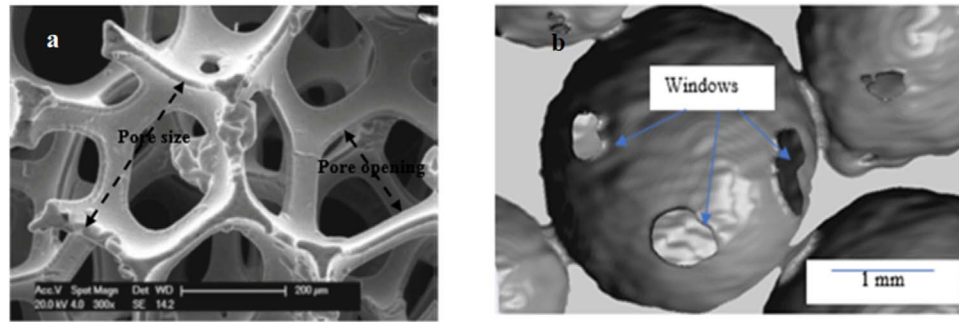
Figure 1. (a) Micrographs of an open-celled porous metallic structure, reproduced from [26]. CC BY 4.0 and (b) is the tomography image showing the typical cell sizes and pore openings of 'bottleneck-type' structures, reprinted from [9], Copyright (2016), with permission from Elsevier.

the mechanical compression of porous samples can result in the deformation and change in the internal topology of the porous structures approximated by lots of imperfect cells [19, 24, 25]. This is also accompanied by reduced cell size, pore openings, and pore-volume and an increase in the surface area and nonuniformity of pores in the materials.

Generally, the transport of fluids across porous media can be described by the well-established Darcy's model in equation (1). This equation relates the unit pressure drop (∇P) developed across porous structures as a function of superficial fluid velocity (v_s). The equation was developed to account for the hydraulic conductivity and permeability of water flow in packed beds and was reported in [27–32] for very slow fluids, typically, for system characterised by pore-diameter Reynolds numbers (R_{ED}) below unity. Quadratic (equation (2)) and cubic (equation (3)) terms were proposed by Phillipe Forchheimer (1901) [28–39] to account for the inertial effects in high and extremely high-gas flow velocity in porous media respectively. The power-law term was also proposed in [35, 40] to describe high-gas flow velocity (equation (4)).

$$\nabla P = \alpha v_s \tag{1}$$

$$\nabla P = \alpha v_s + \beta \rho v_s^2 \tag{2}$$

$$\nabla P = \alpha v_s + \beta \rho v_s^2 + \gamma \rho^2 v_s^3 \tag{3}$$

$$\nabla P = \alpha v_s^n \tag{4}$$

$$\alpha = \frac{\mu}{k_o}, \ \beta = C = \frac{C_F}{\sqrt{k_0}} \ \& \ \mu = \sigma_D.\mu_t \tag{5}$$

where α is the viscous term, β or C is the inertial term also known as Form drag, C_F is the Forchheimer coefficient, k_0 is the permeability of the porous medium, n is power index (constant), μ is the fluid dynamic viscosity. The relationship between the fluid dynamic viscosity (μ) and void eddy viscosity (μ_t) was proposed in [41] using local averaging time velocity to account for the ratio of Darcy's law to turbulent flow (σ_D). Experimental measurements of pressure drop across packed beds in [33] justify the validity of the Forchheimer cubic's model to reliably represent their data. However, several research works on fluid transport in packed beds have reported [16, 28, 30] the preferential applicability of the Forchheimer quadratic model (equation (2)) to fully describe measured and modelled data of unit pressure drop as a function of superficial fluid velocity. More so, the transport of fluid in porous metallic structures in [1–3, 8, 19, 39, 40, 42] confirmed the reliability of the Forchheimer quadratic model to fully describe the flow behaviour in these materials. This has proven useful in accounting for the two most important parameters (permeability, k_0 and Form drag, C) of flowing fluid in porous metals varying in degree of cell size, pore openings, interstices, and pore morphology.

Altering the microstructural arrangement of porous metallic structures can be acheived [8, 19, 43–47] by hole-drilling, mechanical compression, and rolling techniques. These techniques have been adopted in [19, 44] to change the structural morphology of highly porous open-celled (Inconel and Recemat) samples and low-density closed-celled Alporas foams (produced by gas injection of liquid melt [45]). Similar technological approaches have also proved useful in changing the structural topology of 'bottleneck-type' structures in [6, 13]. These techniques have the potential to significantly influence the pore-structure related properties (porosity, surface area, pore-volume, morphology, pore diameter sizes, and pore openings) and fluid flow (velocity and pressure fields) behaviour of porous matrices. Because of this, both the viscous (permeability, k_0) and inertial (Form drag coefficient, C) terms in the Forchheimer model (equation (2)) are greatly affected. However, these approaches are economically expensive and further complicate the skeletal configuration of the porous structures. Therefore, adopting reliable, more cost-effective and more convenient modelling routes capable of

replicating the structure and their flow properties are highly desirable. However, these modelling routes must also be adaptable to accurately represent the geometrical features and fluid dynamics (during modelling) to predict the measured flow data of porous media.

Simplified and idealized geometrical models to reproduce the shape and morphology of porous metallic structures have been developed previously with the aim of capturing important characteristics of the porous matrix, typically, cell sizes, shapes, and openings. Cardinal examples are Lord Kelvin [48] and Weaire-Phelan (W-P) [49] unit cell representation of porous structures. Kelvin [48] proposed a 'virtual' representation of packed structures (an inverse of this becomes a virtual-replica of porous metals) to be a polygon with eight non-planar hexagons of no net curvature and six planar quadrilateral faces. Weaire and Phelan (1994) [49], developed the W-P cell structure that reduces the surface energy of Kelvin's cells by 0.3% and consists of a tetrakaidecahedron with twelve pentagonal faces and two hexagonal faces and an irregular dodecahedron with pentagonal faces. Space-filling of cellular solids (cuboids or cubes) was proposed in [50], cylindrical structures for heat transfer in [46], a rectangular prism for high porosity flow in a porous metallic structure in [51], and a virtual reconstruction of open-cell foams with circular and triangular struts for a deeper understanding of transport phenomena therein [52]. Attempts were made in [9, 11, 53, 54] to create 'virtual' macroporous structures generated by sphere-packing models to understand the fluid flow behaviour and non-acoustical properties of 'bottleneck-type' structures.
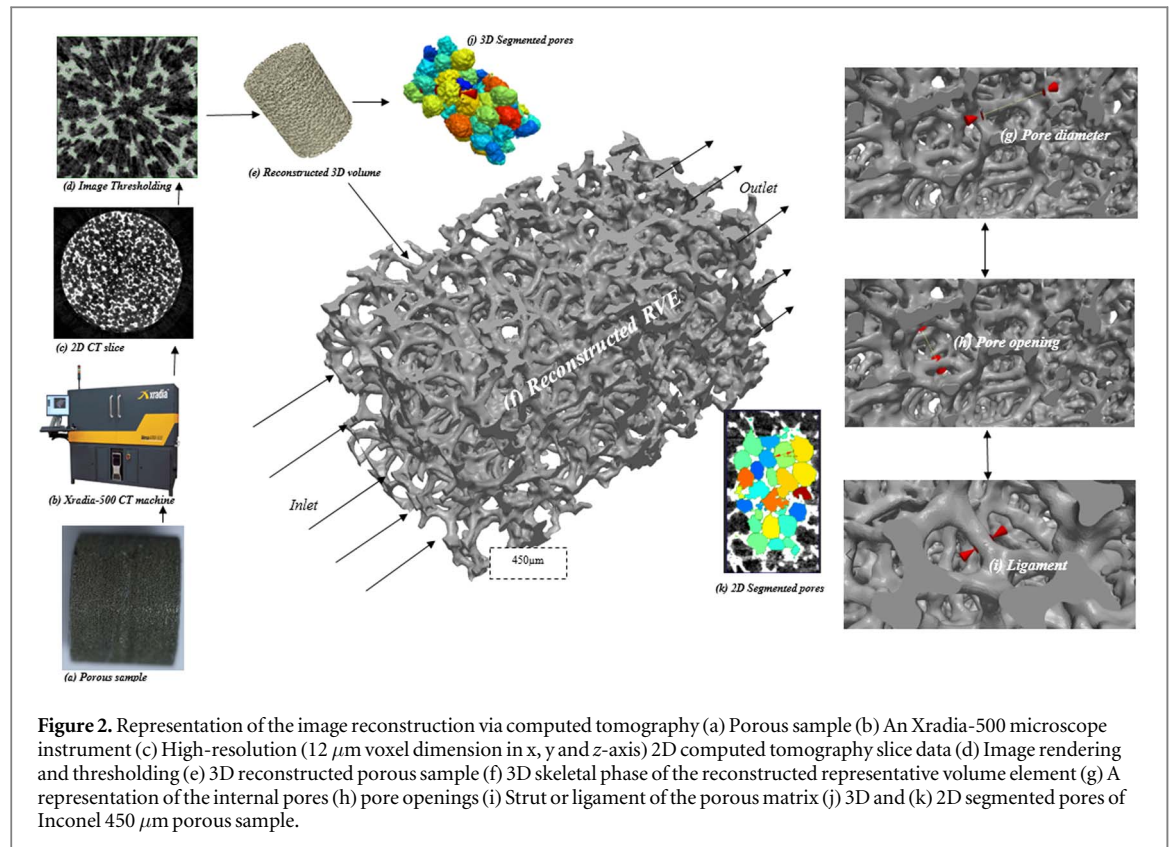
Measurements using optical microscope techniques that measure cell diameter, strut thickness, pore connectivity or 'window', cell volume and many other features have been used [55, 56] to reveal structural information for application specific porous materials. Measuring foam features manually using traditional optical microscope techniques can be time-consuming, labour intensive and limited to capturing only surface information and often requires the destruction of samples because of their complicated three-dimensional (3D) structure [57]. These parameters are difficult to measure using traditional techniques which have been mostly adopted in medical and engineering applications. x-ray computed tomography (μCT) has been used in several applications ranging from material research [58–63] to reverse engineering of complex parts with high precision. Pore-level characterization and computational fluid dynamics modelling and simulation of fluid flow through a representative highly-porous (porosity ranging between 80 and 95%) metallic structures in [62–69] have seen the utilization of high-resolution tomography datasets. This approach provides a more visceral assessment and characterization of foam structures [66] but represents a time-consuming and costly approach [52, 66] and modelling results can often deviate significantly when working with low-resolutions scans [67].

Analogus work reported in [16] provides a detailed analysis on the estimation of pore structure and flow information of 'bottleneck-type' structures using tomography datasets; an extension to structural erosion of the materials to create more highly porous 'bottleneck' structures. However, fluid flow behaviours across 'bottleneck' structures (figure 1(b)) are in many ways different from commercially-available highly-porous materials. These highly-porous metallic materials are reportedly characterised [42] as 'tetrakaidekahedron-shaped' with high pore-volume and consistent pore-uniformity resulting in the creation of less energy within the pore-walls [15]. In addition, the transition in the relaxation behaviour at the scale of the near-circular pore walls of the 'bottleneck-type' structures [15] contributes to the significant amount of energy created within these structures [70]. This paper, therefore, fully addresses the influence of geometrical architecture on the local velocity and pressure dispositions for a moving fluid across a 'tetrakaidekahedron-shaped' highly-porous metals (figure 1(a)). This work is distinguished from [16, 42] with a detailed understanding of the flow pathways in microcellular structures that would have been difficult to handle experimentally. This led to the establishment of appropriate regime of manifestation of moving fluid across these structures and a useful relation between fluid flow properties and pore-structure related parameters of the porous medium.

2. Research approach

This study adopts a similar modelling approach reported in [1, 2, 68, 69] to reconstruct representative structure of porous metallic foams for pore-structure characterisation and computational resolution of the local and pressure drop therein. A Zeiss Xradia Versa XRM-500 3D x-ray CT microscopy system (figure 2(b)) was used to acquire tomography datasets (figure 2(c)) of highly-porous metallic samples (figure 2(a)) with voxel dimensions ranging between 12 and 26 μm resolution in the x, y, and z planes. These materials are Inconel 450 μm, Inconel 1200 μm, Recemat RCM-NCX 1723, Recemat RCM-NCX 1116 and Porvair 7PPI foams.

The Scan IP module of Synopsis-Simpleware^{TM} (a 3D advanced image processing software) was used to render 2D greyscale tomography data (figure 2(c)) into a 3D volume (figure 2(e)). A subvolume rectangular-shaped representative volume element (RVE) that is 6–12 times the mean pore-size of the structures were extracted from the center of the large 3D samples within the ScanIP, to ensure that the representative subvolume was a close representation of the respective full samples. The size of which was determined by reducing a volume

Figure 2. Representation of the image reconstruction via computed tomography (a) Porous sample (b) An Xradia-500 microscope instrument (c) High-resolution (12 μm voxel dimension in x, y and z-axis) 2D computed tomography slice data (d) Image rendering and thresholding (e) 3D reconstructed porous sample (f) 3D skeletal phase of the reconstructed representative volume element (g) A representation of the internal pores (h) pore openings (i) Strut or ligament of the porous matrix (j) 3D and (k) 2D segmented pores of Inconel 450 μm porous sample.

until the porosity differed by $\pm$2% from the 3D full sample. This approach was compared to a more robust and highly computational approach to determine an RVE based on isotropic flow computations for a linear pressure variation (LPV), impermeable side wall (ISW) and solid sidewall (SSW) boundary conditions with reasonable agreement to extract the RVE from the centre (>30% of the total volume) of the porous structures. The selection of lower pore volume (below 6 x cell sizes) may be favourable in terms of resolving computationally, considering time and convergence, but the perceived inability to accurately capture the complete information necessary to represent the entire volume may significantly deviate the modelling accuracy. It is therefore imperative to estimate a workable volume that reliably describes the flow behaviour of the full sample.

The extent of thresholding also has resultant effects on the topology of the microstructures and their macroscopic parameters. Thresholding below the nominal porosity value (measured in ScanIP) of the foam structures separates the pores from each other, resulting in the reduction of their capillary interaction (between connecting pores), pore-openings, pore-sizes, and bulk volume. This results in the reduction of the permeability (computed in +FLOW module of Simpleware^{TM}) by more than half the value of the 'real' structure and an increased specific surface area of the microstructural arrangement. Thresholding above the nominal porosity increases the pore-openings and in turn, increases the bulk volume and permeability. Care was taken to ensure that minimal deviations between the porosity of the processed 3D representative volume only differed by $\pm$ 2% from the nominal porosity of the full samples. The nominal porosities of the full samples were determined using a mass scale differential approach with the aid of a smart weight digital scale and a vernier caliper. Structural parameters like porosity, pore-volume, skeletal volume, and skeletal surface area of the representative structure were measured directly in ScanIP module of the 3D advanced imaging software. The mean pore diameter size was obtained by a watershed segmentation process (separating particles, figures 2(j), and (k)) of Boolean inverted skeletal matrices (to obtain the fluid domain) where a mean value was extracted. Additionally, the mean pore openings were determined by creating a centreline which runs through the openings and pores of the structures and was used to compute the mean diameter pore-diameter openings. Structural erosion and dilation of the representative samples were also carried out in the ScanIP to create 'semi-virtual' structures (to be discussed later in detail). Figure 2 presents images obtained from the 3D advanced image processing of an Inconel 450 μm porous metallic structures working from a high-resolution (12 μm voxel resolutions) tomography datasets.

Computational fluid dynamics (CFD) modelling and simulation of an airflow across these structures were made possible by solving the steady-state fluid equations on the inverse of the representative skeletal frame (i.e. fluid domain) of the porous structures for velocities in the range of 0 and 6 m.s^{-1}. This numerical simulation was carried out in the CFD module of COMSOL Multiphysics 5.2^{TM} software. The well-established Navier–Stokes equation (equation (6)) was solved for slow and laminar fluid velocities while the Algebraic yPlus Reynolds

Average Navier–Stokes (RANS) model (equation (7)) was solved for the high fluid velocity, to account for the eddy viscosities (μ_t) that add up to the molecular viscosity. Resulting pressure drop for this low-Reynolds turbulence model was observably close (R$^{2\sim}$ 0.996) to the application of the Spalart-Allmaras RANS Turbulence model used in [2] for resolving fluid flow in highly porous metallic structures. This close proximity in computed pressure drop values obtained using the selected RANS turbulence models could be due to their flexibility to resolve low—moving fluid in wall—bounded flows [71]. The specification of low and high fluid velocities was done using the concept of pore-diameter Reynolds number approach proposed in [24]. Typically, values below 300 are considered laminar, otherwise, turbulence. For the preservation of continuity [62, 72], an inlet pore-velocity (v_p) was applied. The pore fluid velocity (v_p) was achieved by dividing the seepage or superficial fluid velocity (v_s) by the porosity (ε) of the porous structures. Also, the walls of the struts are no-slip walls taking into account a zero pressure at the outlet and symmetrical boundary condition on the remaining facets of the representative matrix.
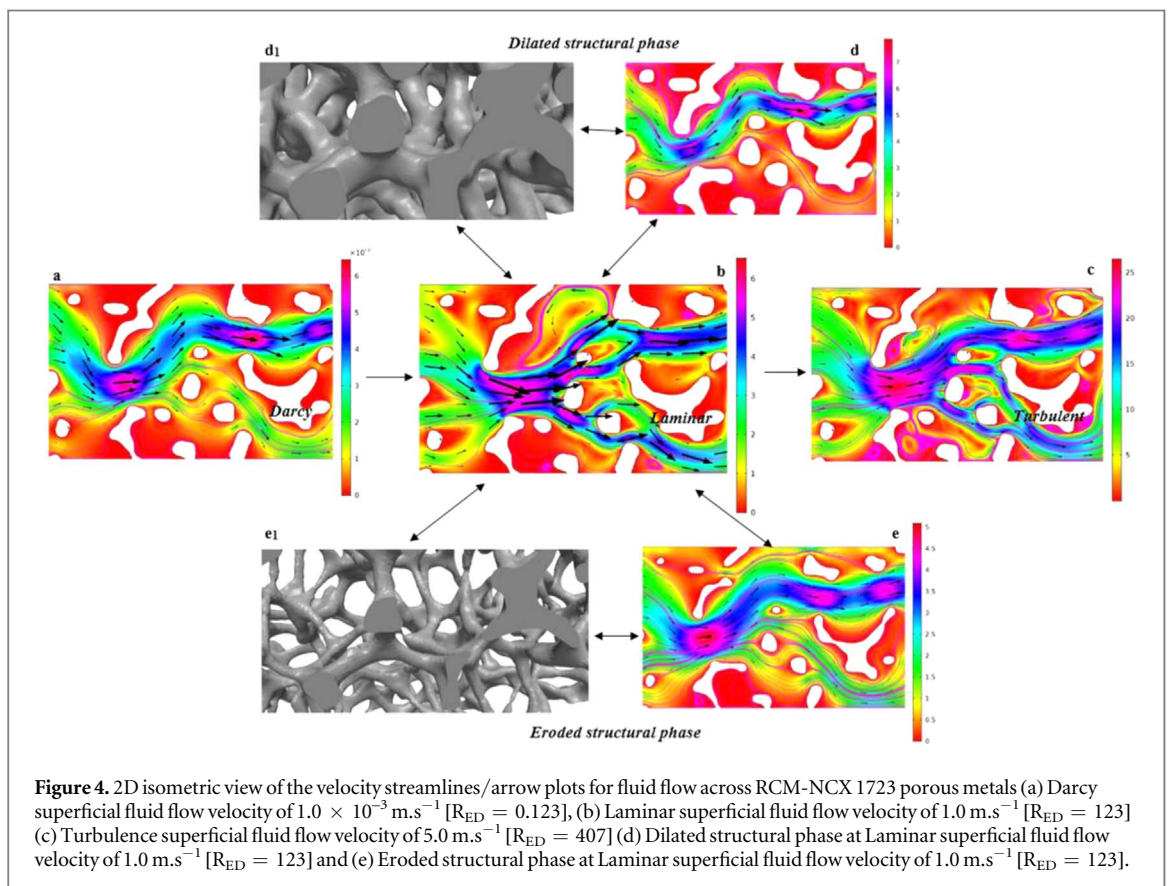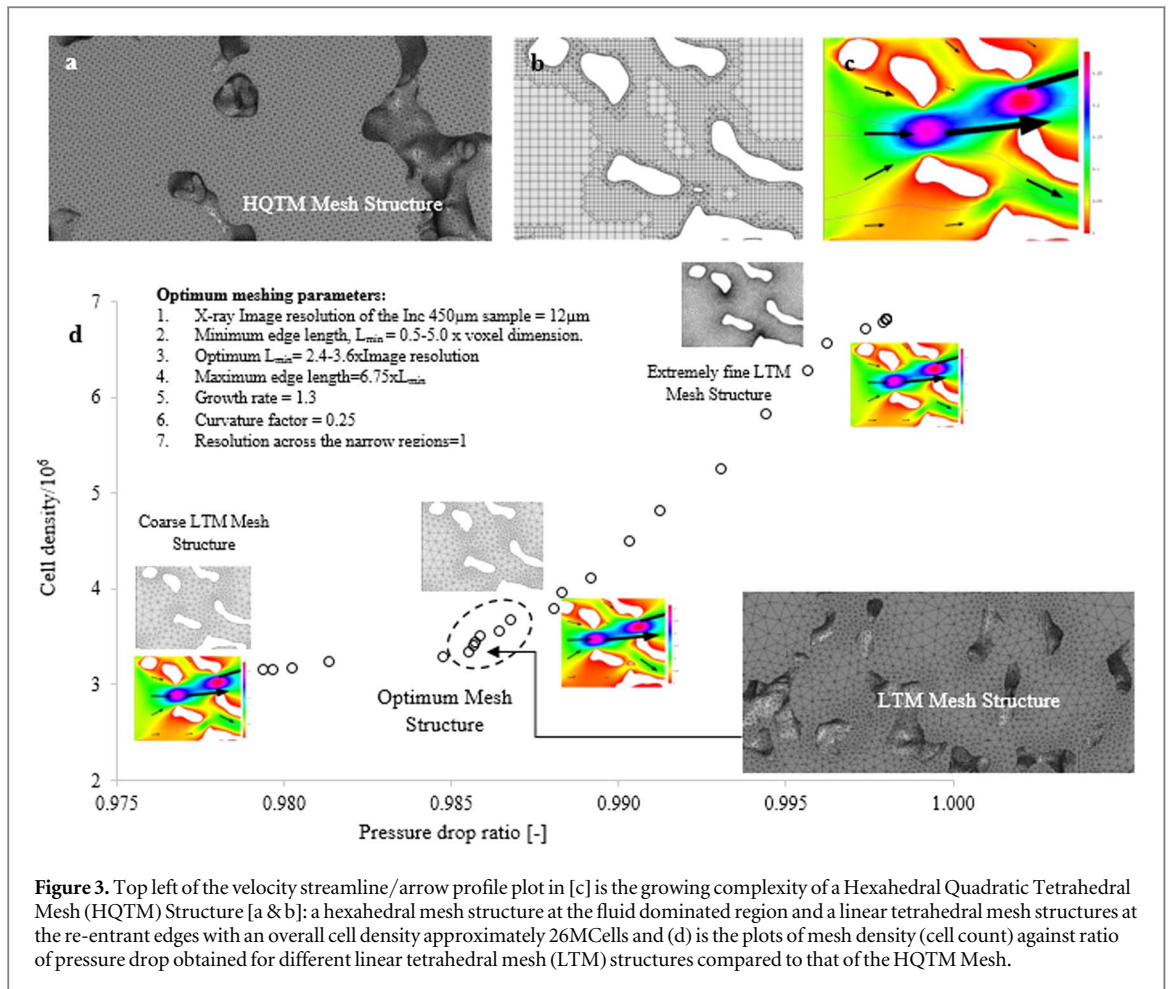
$$\underbrace{\rho\frac{\partial v}{\partial t} + \rho(v.\nabla)v}_{Acceleration} = \underbrace{-\nabla p + \mu\nabla^2 v + \nabla(\lambda + \mu)(\nabla.v)}_{Force\ due\ to\ velocity\ gradient\ and\ pressure} + \underbrace{F}_{Force\ due\ to\ external\ field} \qquad (6)$$

$$\underbrace{\rho\frac{\partial v}{\partial t} + \rho(v.\nabla)v}_{Acceleration} = \underbrace{\nabla.[-p + (\mu + \mu_t)(\nabla v + (\nabla v)^T) - \frac{2}{3}\nabla(\mu + \mu_t)(\nabla.v)}_{Force\ due\ to\ velocity\ gradient\ and\ pressure} + \underbrace{F}_{Force\ due\ to\ external\ field} \qquad (7)$$

Detailed information of the velocity and pressure fields of the moving fluid across the interstices of the porous structures were made possible through a workable application of an elementary mesh-scale dependent study performed with an increasing level of details until the independence of the flow information in respect to the cell density was established. A linear tetrahedral mesh (LTM) was applied to the 3D fluid domain of the representative Inconel 450 μm porous structure within the +FE module of Simpleware^{TM}. A growth rate of 1.3 was applied on this domain to grow the tetrahedral cells from the re-entrant edges leading to the large concentration of smaller-sized cells within the pore-openings of the microstructure (figure 3(b)). The smaller-sized cells were determined by varying the minimum edge length between 0.5 and 5.0 times the voxel sizes whilst the maximum cell sizes (largely concentrated at the center of the pores) were set to be 6.75$\times$ the minimum edge length value (figure 3). Computed pressure drops values obtained using the specified range of minimum edge and maximum LTM mesh length were compared to that obtained using a highly dense hexahedral quadratic tetrahedral mesh (HQTM) structure (figure 3(a)) that could be solved computationally in the +FLOW module of Synopsis-Simpleware^{TM}, within the available PC specification. This comparative approach is imperative to efficiently resolved microscale simulation results of sufficient size to yield a acceptable margin of a macroscale system [73]. It is important to understand that the HQTM mesh structure (predominantly hexahedral with fewer tetrahedral meshes at the walls [74]) is formed by creating a conformal alteration to the unrefined part of a mesh by splitting the neighbouring elements to eliminate hanging nodes [75]. Though, this type of mesh structure is computational demanding to resolve in commercial CFD software due to its high degree of freedom (mesh density close to 30 Mcells for 3D RVE Inconel 450 μm sample) requiring high memory usage and computational time. Most commercial CFD software uses the Taylor-Hood P$_2$-P$_1$ elements (quadratic elements for the velocity and linear element for pressure) for their computation. By default, the stabilized P$_1$-P$_1$ elements (linear for both the velocity and pressure computations) reduces the number of unknowns and makes computation faster with less memory utilization is used in the +FLOW solver of Simpleware^{TM} [76, 77] for fluid flow computation. figure 3(d) presents a plot of the mesh density (Mcells) against the ratio of computed pressure drop using the LTM mesh structure to that of HQTM mesh structure. This shows a less than 3 percent negligible benefit to reduce the smaller-sized mesh structure to below 2$\times$ voxel dimension ($\geqslant$4.0 M-cells) when compared with the consequence of computational time, which is more than 10$\times$ longer than having a minimum edge length between 2.4–3.6$\times$ voxel dimension.

3. Analysis of research data

The pattern of fluid flow across the 'real' and 'adapted' structures and their regime of manifestation can be easily interpreted using two-dimensional plots of a RCM-NCX 1723 porous sample. Figure 4(a) presents a two-dimesional (2D) velocity streamline/arrow profile plot for very slow fluid [R$_{ED}$ = 0.123] in the Darcy regime. The 2D velocity profile plots for flowing fluid in the laminar [R$_{ED}$ = 123] and turbulent (R$_{ED}$ = 407) regimes are represented by figures 4(a) and (c) respectively. Figure 4(d) represents a 2D velocity profile plot across 'structurally-dilated' porous (figure 4(d$_1$)). The 2D velocity pattern across a 'structural-eroded' porous sample (figure 4(e$_1$)) is represented by figure 4(e). These adapted structures were created by repeatedly removing (erosion) or adding (dilation) pixel elements to the skeletal matrix of the porous medium; the size of which is
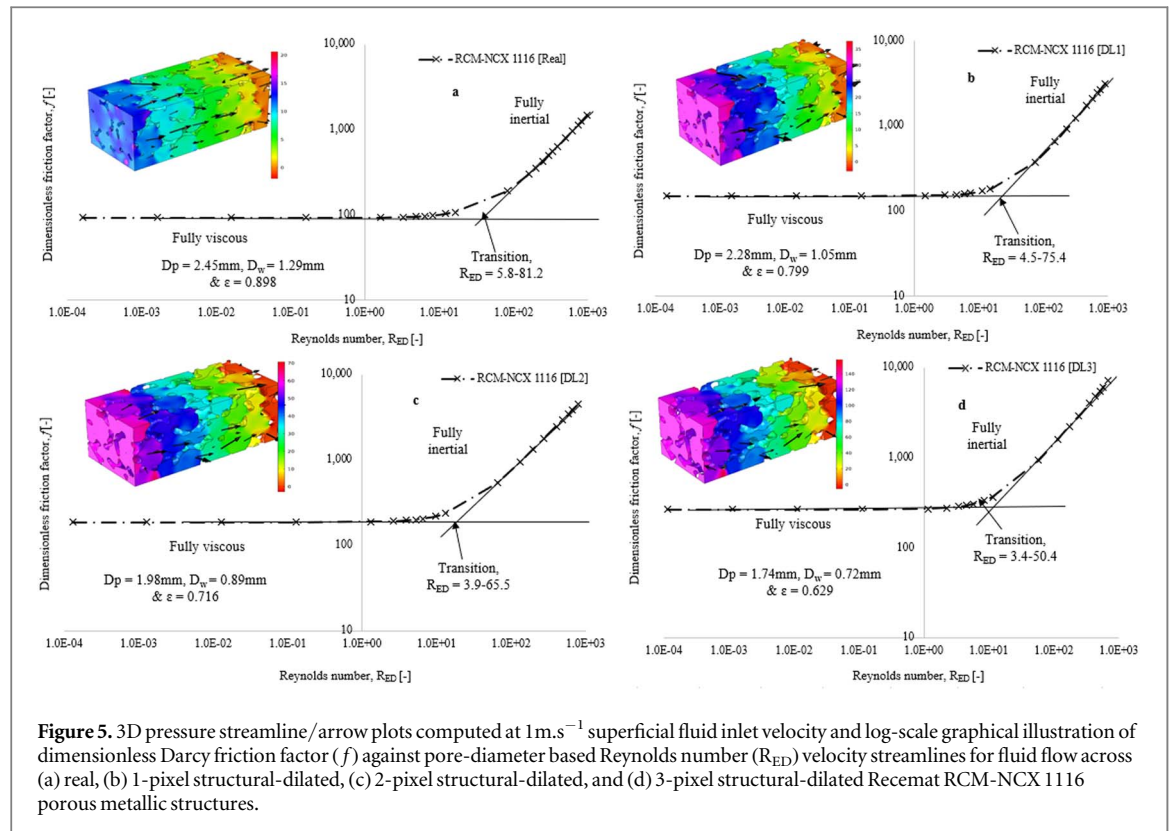
Figure 3. Top left of the velocity streamline/arrow profile plot in [c] is the growing complexity of a Hexahedral Quadratic Tetrahedral Mesh (HQTM) Structure [a & b]: a hexahedral mesh structure at the fluid dominated region and a linear tetrahedral mesh structures at the re-entrant edges with an overall cell density approximately 26MCells and (d) is the plots of mesh density (cell count) against ratio of pressure drop obtained for different linear tetrahedral mesh (LTM) structures compared to that of the HQTM Mesh.

Figure 4. 2D isometric view of the velocity streamlines/arrow plots for fluid flow across RCM-NCX 1723 porous metals (a) Darcy superficial fluid flow velocity of 1.0×10^{-3} m.s^{-1} [$R_{ED} = 0.123$], (b) Laminar superficial fluid flow velocity of 1.0 m.s^{-1} [$R_{ED} = 123$] (c) Turbulence superficial fluid flow velocity of 5.0 m.s^{-1} [$R_{ED} = 407$] (d) Dilated structural phase at Laminar superficial fluid flow velocity of 1.0 m.s^{-1} [$R_{ED} = 123$] and (e) Eroded structural phase at Laminar superficial fluid flow velocity of 1.0 m.s^{-1} [$R_{ED} = 123$].

Figure 5. 3D pressure streamline/arrow plots computed at 1m.s^{-1} superficial fluid inlet velocity and log-scale graphical illustration of dimensionless Darcy friction factor (f) against pore-diameter based Reynolds number (R$_{ED}$) velocity streamlines for fluid flow across (a) real, (b) 1-pixel structural-dilated, (c) 2-pixel structural-dilated, and (d) 3-pixel structural-dilated Recemat RCM-NCX 1116 porous metallic structures.

determined by the resolution or voxel size of the respective tomography datasets. This process gradually changes the pore-structure properties of the material which invariably affects the velocity and pressure fields developed across the sample. This erosion process of adapting structures is reportedly [16] useful in increasing the pore volume of the 'bottleneck-type' structures (figure 1(b)) and provides reasonable fits to experimental scatter. Surprisingly, the application of this process to the highly-porous matrices used herein resulted in a further increase in pore volume and the appearance of lost struts (figure 4(e$_1$)). However, the dilation of the structural-phase of the porous structures (figure 4(d$_1$)) resulted in reduced pore-volume and increased strut thickness. Though, the two-dimesional (2D) approach provides useful information and visualisation of the flow behaviour across the porous structures, however, overall conclusion of their pressure drop data may not be extensible when compared to three-dimensional (3D) representative structures. Observably, simulated values of pressure drop data against superficial fluid velocity for the 2D microscale structures could not provide satisfactory estimates of the 3D macroscale media due to the elongated pore-nonuniformity (tortuosity) and anisotropy of the 3D unit cell [78]. Therefore, flow properties would better be described (to be discussed later) based on the 3D unit cell which reliably describe the pressure and velocity dispositions across all the three different tortuous paths.

Figure 5 presents 3D pressure streamline/arrow plots and the manifestation of fluid from fully viscous to fully inertial regimes for the 'real' (a) and adapted (b–d) RCM-NCX 1116 structures. These adapted structures were created by the addition of (b) 1-pixel (c) 2-pixels and (d) 3-pixels to the skeletal phase of the 'real' porous material. The log-scale plot of dimensionless Darcy friction factor ($f = \nabla P.D_p^2 / [\mu.v_s]$) in [40] against pore-diameter Reynolds number ($R_{ED} = \rho v_s D_p / \mu$) was used to separate the non-linear deviation of flowing fluid from Darcy regime. Similarly, figures 6(a) and (b) compare log-scale plots of the dimesionless friction factor against Reynolds number for the real and dilated RCM-NCX 1116 structures. Figure 6(b) is distinguished from figure 6(a) by using permeability ($k_0 = D_p^2$) as the characteristics linear dimension of the porous structures, as substantiated in [39, 79]. Figure 5 shows that the transition from Darcy to laminar is gradual and a sharp change near the pore-walls in figure 4(b) was observed, indicating the onset of inertial and formation of eddies (figure 4(c)). These eddies are created by the presence of normal and tangential shear stresses within the pore-walls and moving fluid, stretched by increased velocity gradients [80, 81]. At higher pore-diameter Reynolds number (typically in the turbulence regime), fluid flow within the porous matrices was largely characterised by the rapid movement of fluid particles developed across the interstices of the structures (figure 4(c)). This affirms that the onset of turbulence is not just characterised by high-fluid velocity but also the formation of an unsteady pattern of eddies [82]. The erosion of the skeletal-frame of the porous structure resulted in an increased pore volume (figure 4(e$_1$)) thereby reducing the flow eddies (recirculation effects) and forcing a stable streamline flow within the material (figure 4(e)). Conversely, continuous dilation of the skeletal-frame (figure 4(d$_1$)) resulted in
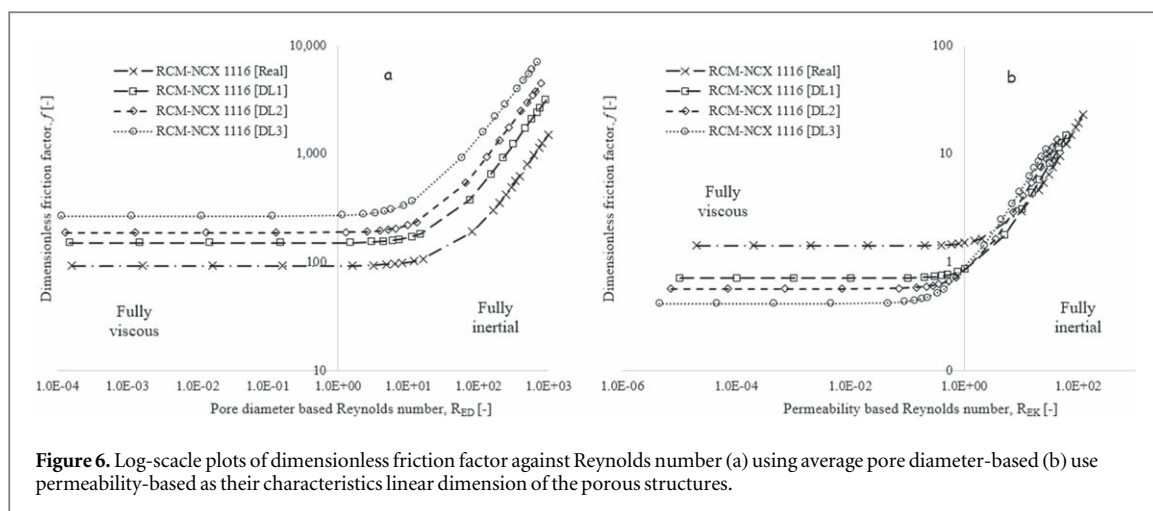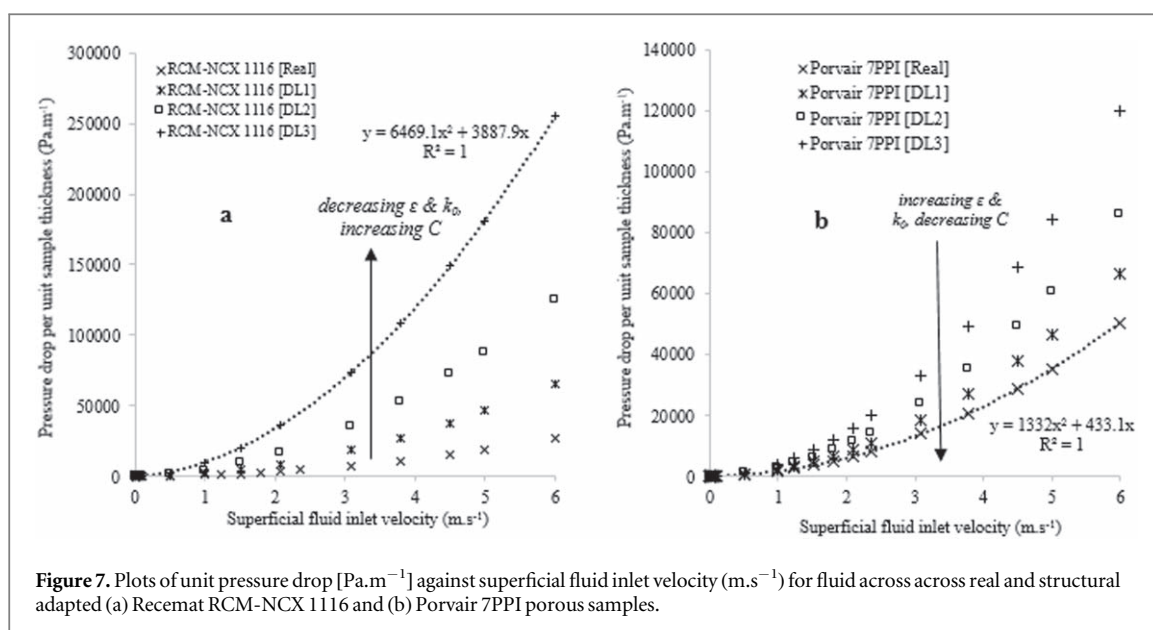
Figure 6. Log-scacle plots of dimensionless friction factor against Reynolds number (a) using average pore diameter-based (b) use permeability-based as their characteristics linear dimension of the porous structures.

an unsteady pattern of fluid flow which invariably increases the dissipated energy [82, 83] and drag formation [16, 19] between the moving fluid and pore-walls.

Weak oscillations characterised by stability in streamlines of fluid motion were largely observed for fluid flow in the Darcy regime (figure 4(a)). Figure 5 shows that the fluid flow within this regime is predominantly viscous thereby indicating the absence of eddy viscosity (figure 4(a)) and a linear dependence of pressure fields on the velocity gradient was observed [84, 85]. The recirculations of the fluid within the pore-openings were quite evident in figure 4; they grow in size and number as the fluid velocity transition from Darcy to turbulence. This shows the ability of the flowing fluid to fully penetrate the geometrical architecture of the porous structures at high fluid velocities. At very slow Darcy velocities (figure 4(a)), the movement of fluid was mainly through preferential openings normal to the preceding pore-openings and less for the tangential pore-openings. At high fluid velocity, unstability in the laminar flow of fluid was observed and a transition to turbulence took place. Flow separations from the particles combined with instability in streamline flow were observed at the onset of inertial (transition regime). The increase in fluid velocity resulted in the penetration of more tangential pore-openings by the moving fluid. Hence, more chaotic and random motion of the fluid within the porous matrices were quite evident within the pore structures. Figure 5(a) showed that the pore-diameter Reynolds number for the existence of fluid transition from fully viscous to fully inertial in the 'real' RCM-NCX 1116 sample ranges between 5.8 and 81.2. A gradual decrease in transition regime was observed for the dilated structures as shown in figure 5(b)—(d). Observably, the onset of inertia decreases with decreasing pore-volume, highest and lowest for porosities of 89.8 and 62.9% respectively. The decreasing trends in the transition Reynolds number may be attributed to the high surface roughness and topology of the dilated porous structures. Intriguingly, related works of fluid flow in porous media in [28, 83, 86, 87] defined the non-linear departure of fluid from Darcy to Forchheimer to be between 1 and 10. However, their studies were based on fluid flow across packed beds characterised by much lower pore volume fraction, typically, between 0.33 and 0.48 for dense and loosed packings respectively [30]. Moreso, experimental measurements of flow properties in high porosity foams in [88] provided the departure from Darcy to be between 14 and 27 and this could support the reliability of the CFD modelled data presented herein. Figures 6(a) and (b) show that consistent changes to the pore-diameter Reynolds number to a value below unity can be achieved by continuously decreasing the available pore spaces (addition of more pixels to the skeletal phase) within the porous matrices. Both plots exhibit similar behaviour of linear description of flow laws in tha Darcy regime and an onset of inertial leading to non-linearity deviation at high fluid velocity. Using the permeability as the characteristic linear dimension, the onset of deviation from Darcy was observed for Reynolds number beyond 1.5 for the real foam and less than unity for all the dilated structures.

Figure 7 presents the plots of CFD computed unit pressure drops developed across 'real' and 'adapted' porous samples (**a**, RCM-NCX 1116 and **b**, Porvair 7PPI foams) against superficial fluid inlet velocity. The Forchheimer quadratic model (equation (2)) reliably described the flow information for all the structures (figure 7) and was used to estimate the permeability and Form drag information of the porous structures. Analgous research works in the field of transport in porous media favour the Forchheimer quadractic model (equation (2)) for 3D materials whilst most of the results in favour of the cubic model (equation (3)) are for 2D materials. Also, to ensure positive entropy generation production for all Reynolds number, the quadratic term in the Forchheimer model must preserve the sign of velocity [73]. Table 1 presents the pore-structure related and flow information of both the 'real' and 'adapted' RCM-NCX 1116, Porvair 7PPI and Inconel 450 μm structures. Despite characterised by similar porosities, the pressure drop across the 'real' sample was observably high for the

Figure 7. Plots of unit pressure drop [Pa.m^{-1}] against superficial fluid inlet velocity (m.s^{-1}) for fluid across across real and structural adapted (a) Recemat RCM-NCX 1116 and (b) Porvair 7PPI porous samples.

Porvair 7PPI foam and low for the 'real' RCM-NCX 1116 sample. This is largely attributed to the low pore openings of the Porvair 7PPI foam; this is reported in [2, 19] to have a resultant effect on the permeability of the porous medium. Table 1 shows that the computed permeability value is smallest for the 'real' Inconel 450 μm sample. Interestingly, this is the structure characterised by having the smallest pore openings of 240 μm (table 1). Conversely, the Form drag of these materials were observably highest for the structure with the lowest openings and lowest for structure with the largest openings. Continuous dilation of the skeletal frames of the porous matrices resulted in increased strut thickness and surface area of the structures. This change in the pore-structure properties has an overall effect on the viscous and inertial terms of the moving fluid. At high fluid velocity, significant amount of kinetic energy is lost as fluid traverses the interstices of the porous structures [89]. Figure 4(c) seemingly described this unstable pattern of flow eddies of flowing fluid in the porous structure at high superficial fluid flow velocity. These eddies increase with reduced cell sizes (figure 4(e)) thereby resulting in an increase in the normal and tangential shear stresses existing between the flowing fluids and the skeletal walls.

Table 1 shows that the Form drag (C) increases with a consistent decrease in the pore-size (increase in surface area and ligament thickness). More so, pressure drop developed across the 'adapted' structures were observably higher when compared to the flow information of the 'real' structures. Highest for structures with the highest voxel addition and lowest for structures with the no voxel addition (real samples). The influence of pore-structure related properties of the porous matrices was further substantiated by plotting a dimensionless reduced Darcian permeability ($k_{RP} = \varepsilon^3.k_0/r_p^2$) and reduced Form drag ($C_{RP} = \varepsilon^{-4}.C.r_p$) against their pore-volume fraction (ε). Figure 8(a) presents such plots for both the combined 'real' and 'adapted' structures. This shows a direct and inverse power law relation for the reduced Darcian permeability and reduced Form drag respectively. The power-law relation between the reduced terms clearly provides the best fits to the modelled data with less than 4 percent tolerance limits for both the viscous and inertial terms. Figure 8(a) also presents the flow behaviour of highly-porous and semi-open and close-celled porous metallic structures. The highly-porous open-celled structures are characterised by high pore-volume fraction, typically, above 0.72, high flow permeability and low Form drag. Conversely, the close-celled cellular structures are characterised by low pore-volume fraction, typically, below 0.66, low permeability and high Form drag. Structures with intermediate pore volume fraction, typically, between 0.66 and 0.72 could be regarded as semi-open celled structures. In agreement with these specifications, related works in [4–7] specified the pore volume fraction of highly-porous metallic structures to be within the range of 0.75 and 0.95. In addition, structures characterised by low pore-volume fraction, typically, below 0.66 are classified as close-celled structures [1, 3, 13, 14, 20, 23]. Such low-porosity porous structures are either achieved by mechanical compression of the highly-porous metallic structures [20, 23] or replication casting of near-spherical beads at high applied differential pressures needed to drive liquid metals into the voids created by the beds [13, 42].

The modelling confidence of this pore-scale computational approach was substantiated by making comparison with experimental measurements available in the literature. Figure 8(b) presents the CFD predicted and experimental measurements of unit pressure drop developed across Inconel 450 μm [19] and Inconel 1200 μm [26, 90] samples. Table 2 presents CFD predicted values for permeability and Form drag along with experimental measurements of similar properties obtained by fitting measured pressure data (for similar range

Table 1. Pore-structure related and flow information of the 'real' and 'adapted' RCM-NCX 1116, Porvair 7PPI and Inconel 450 μm porous samples.

μCT Sample	Dp (mm)	Dw (mm)	ε (%)	L_T (mm)	σ_{FB} (mm^{-1})	σ_{FF} (mm^{-1})	Viscous $k_0/10^{-09}$m^2 Darcy	Inertial C (m^{-1})	C_F [−]
RCM-NCX 1116 [Real]	2.45	1.29	89.81	0.34	1.52	13.28	65.36	594.66	0.18
RCM-NCX 1116 [DL1]	2.28	1.05	79.97	1.58	1.82	7.25	34.41	1420.19	0.22
RCM-NCX 1116 [DL2]	1.98	0.89	71.64	1.70	2.27	5.73	20.83	2665.06	0.38
RCM-NCX 1116 [DL3]	1.74	0.72	62.85	1.83	2.78	4.70	10.99	5369.88	0.37
Porvair 7PPI [Real]	1.47	0.86	89.69	0.41	2.25	19.60	25.14	1105.67	0.23
Porvair 7PPI [DL1]	1.43	0.80	85.83	1.48	2.38	14.45	19.96	1455.72	0.27
Porvair 7PPI [DL2]	1.33	0.75	82.03	1.54	2.66	12.16	15.86	1894.16	0.31
Porvair 7PPI [DL3]	1.23	0.71	78.05	1.61	3.00	10.66	12.10	2651.86	0.39
Inconel 450 μm [Real]	0.45	0.24	83.54	0.06	8.63	43.82	1.25	8541.55	0.34
Inconel 450 μm [DL1]	0.35	0.17	70.54	1.72	11.89	28.49	0.48	29190.67	0.64
Inconel 450 μm [DL2]	0.29	0.12	57.50	1.90	15.37	20.80	0.16	98884.37	1.22

where DL1, DL2, and DL3 are symbols for the adapted-structures created by adding 1, 2 and 3 voxels to the skeletal phases of the materials respectively. Dp $= 2r_p$ is the mean cell sizes (m), r_p is the mean cell radius (m), Dw is the mean pore openings (mm), ε is the porosity (%), L_T is the strut or ligament thickness (mm), σ_{FB} is the structure surface area per unit bulk volume (mm^{-1}), is the σ_{FF} is the structure surface area per unit structure volume (mm^{-1}), k_0 is the Darcian permeability (m^2), k_F is the Forchheimer permeability (m^2), C is the Form Drag (m^{-1}) and C_F is the Forchheimer coefficient [-].
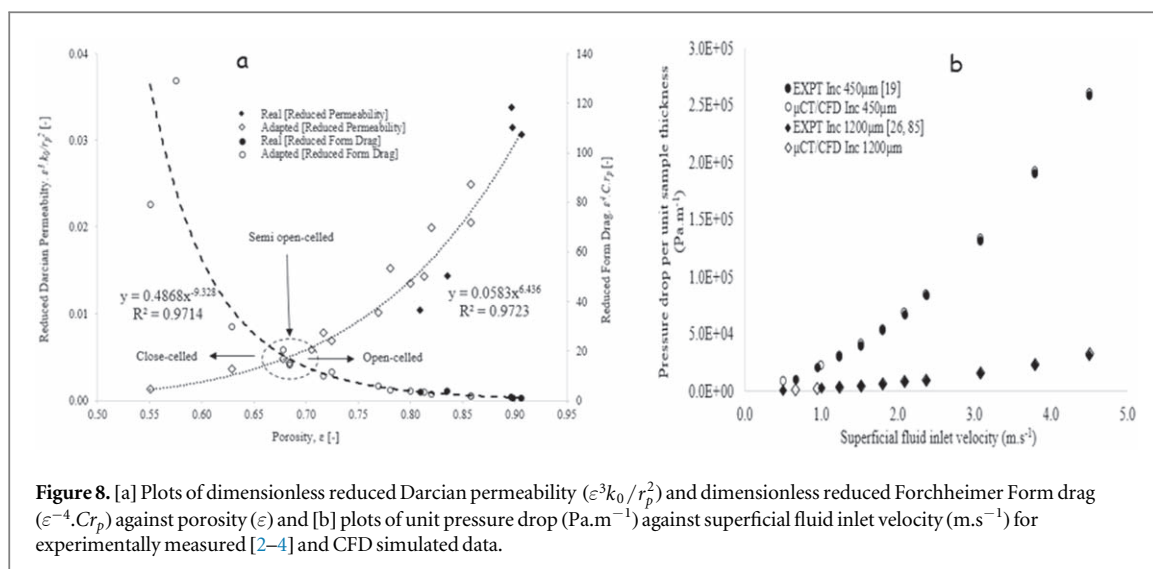
A J Otaru and M B Samuel

Figure 8. [a] Plots of dimensionless reduced Darcian permeability ($\varepsilon^3 k_0/r_p^2$) and dimensionless reduced Forchheimer Form drag ($\varepsilon^{-4}.Cr_p$) against porosity (ε) and [b] plots of unit pressure drop (Pa.m^{-1}) against superficial fluid inlet velocity (m.s^{-1}) for experimentally measured [2–4] and CFD simulated data.

Table 2. Experimentally measured and predicted data of permeability and Form drag.

				Experimental		Predicted	
	Sample/PPI	ε	Dp	k_0 [m^2]	C [m^{-1}]	k_0 [m^2]	C [m^{-1}]
Oun & Kennedy [19]	Inc. 450 μm	0.840	450 [μm]	1.69×10^{-09}	8317.8	1.59×10^{-09}	8283.2
De Carvalho *et al* [26]	Inc. 1200 μm	0.900	1200 [μm]	2.20×10^{-07}	1078.5	2.10×10^{-07}	1131.6
Calmidi & Mahajan [95]	10PPI	0.949	3.13 [mm]	1.20×10^{-07}	—	1.19×10^{-07}	—
	20PPI	0.954	2.70 [mm]	1.30×10^{-07}	—	0.91×10^{-07}	—
	20PPI	0.901	2.58 [mm]	0.90×10^{-07}	—	0.70×10^{-07}	—
Kamath *et al* [96]	10PPI	0.950	4.91 [mm]	2.48×10^{-07}	94.98	2.90×10^{-07}	258
	20PPI	0.900	3.42 [mm]	2.18×10^{-07}	208.82	1.20×10^{-07}	499
	30PPI	0.920	2.324[mm]	1.64×10^{-07}	148.97	0.59×10^{-07}	653
Mancin *et al* [91]	5PPI	0.921	—	2.36×10^{-07}	206	2.83×10^{-07}	297
Phanikumar & Mahajan [92]	5PPI	0.899	4.22 [mm]	1.99×10^{-07}	—	1.80×10^{-07}	—
	10PPI	0.939	3.41 [mm]	1.17×10^{-07}	—	1.37×10^{-07}	—
	20PPI	0.920	2.78 [mm]	1.06×10^{-07}	—	0.85×10^{-07}	—
Bhattacharya *et al* [93]	—	0.899	3.20 [mm]	0.94×10^{-09}	—	1.04×10^{-09}	—
	—	0.937	2.00 [mm]	0.58×10^{-09}	—	0.47×10^{-09}	—
	—	0.909	2.96 [mm]	1.11×10^{-09}	—	0.92×10^{-09}	—

of superficial fluid velocity [0–4.5m.s^{-1}]) in the Darcy-Dupuit-Forchheimer model (equation (2)). The resulting CFD predictions for pressure drop as a test function of superficial fluid velocity were found to be in keeping with equivalent experimentally measured data, with a less than 4 percent deviations. Table 2 also compares predicted values (using analytical expressions of k$_0$ and C in figure 8(a)) with related experimental measurements [19, 26, 91–93] of similar foam properties substantiated in the literature. Although the agreement in permeability with pore-structure variations was small, the disagreement in Form drag were large in some cases, leading to inaccuracies when used to predict C beyond the fluid flow velocity studied herein and for all fluid types and the level of elongation of the tortous pathways. Form drags (C) information in porous media are reported to depend largely on superstitial fluid velocity used to obtained the unit pressure drop developed across the porous samples. Oun & Kennedy [26] reported increasing values of Form drag with increasing superficial fluid velocity from Forchheimer to Turbulent flow regimes. Also, significant correlations for experimentally measured values of C were observed in [26] for different range of velocities in Turbulent regime. Similarly, research findings published in [30] bring strong support to the belief that a generalised model, such as that by Ergun [31, 38], cannot yield a unique value for the inertial coefficient of porous identical packed spheres and there is applicable theory [94] between this inertial coefficient and Form drag information for porous structures.

The extension to structurally adapted 'real' porous samples provide an indepth understanding of the velocity and pressure dispositions within the interstices of the porous structures that may be difficult to characterise experimentally. This could be useful for predicting the viscous and inertial terms (within the studied fluid velocities) of these type of structures with a less than 4 percent tolerance limits for both flow properties. Although, increased computational time was encountered during CFD numerical simulation. This is largely due

to the utilization of high resolution tomography datasets and the adoption of high quality HQTM structures as a basis for comparison with the optimum LTM mesh structures. This was carried out to capture accurate information of the pore-structure based on the computed representative volume at the pore-level. Computational time and convergence observably varies for different structures. These can be largely attributed to the high number of degree of freedom needed to resolve a solution and the pore-velocity of interest. High airflow velocities, typically, in the turbulent regime were observed to be higher than that at the low fluid velocity, typically, in the Darcy regime. Similarly, computational time for the adapted structures was observably lower than the 'real' structures. This is likely due to their high pore volume (lower surface area) requiring more of the larger mesh cell structures at the pores and fewer smaller cells at the re-entrant edges. This reduces their overall mesh density and number of degrees of freedom needed to resolve pressure drops developed across these structures.

4. Conclusions

This work provides a detailed understanding of the velocity and pressure distributions in porous metallic structures working from tomography datasets at the pore-level. This approach led to the determination of pore-structure related parameters and fluid flow information of the porous structure. The following conclusions were drafted from the research:

- The preferential openings of the microstructures were observed to dictate mainly the movement of fluid across their interstices—most especially for very slow moving fluid characterised by weak oscillation and streamline fluid motion. Conversely, recirculation, chaotic movement and increased drag force between the fluid motion and pore walls of the matrices were observed to dominate fast moving fluid.

- The application of flow laws on the CFD predicted pressure data against superficial fluid velocity were used to substantiate the regime of manifestation of flowing fluid from Darcy to inertial for these microcellular structures and a graphical relationship between the pore-structure related parameters and flow properties is substantiated.

- The addition of pixel elements to the skeletal frame of the porous structures further creates virtual structures that is a facsimile of the original structures. This approach lowers the pore volume and pore openings—resulting in high pressure build-up and a more chaotic fluid motion that led to the establishment of turbulence at reduced Reynolds number. Conversely, the removal of pixel elements from the skeletal frame of the porous matrices proved otherwise.

- Acceptable agreements were obtained for the permeability values for all cases and Form drag information, for some cases. These deviations were attributed to the overdependence of the inertial term in the Forchheimer model on the range of superficial fluid velocities, properties of the flowing fluid and the level of elongation of the tortuous pathways. Though further experimental measurements of pressure drops across several porous metallic structures for different types of fluid (both single, multiphase and multispecies) at low and high fluid velocities would be needed to support this claim.

- This approach could assist in understanding the disposition of fluid flow in narrow pathways that may be difficult to characterise experimentally.

Data availability statement

All data that support the findings of this study are included within the article (and any supplementary files).

ORCID iDs

A J Otaru ⓘ https://orcid.org/0000-0002-3057-4991

References

[1] Otaru A J 2019 Enhancing the sound absorption performance of porous metals using tomography images *Appl. Acoust.* **143** 183–9

[2] Otaru A J, Muhammad M S, Samuel M B, Olugbenga A G, Gana M E and Corfield M R 2019 Pressure drop in high-density porous metals via tomography datasets *Accepted for Publication in Met. Mater. Int.* **27** 603–9

[3] Zhou J 2006 Porous metallic materials *Advanced Structural Materials* ed E Winston and O Soboyejo (United States of America: CRC Press, Taylor & Francis Group) p 22

[4] Jorges P A and Malcom J C 2010 Recent-trends in porous sound-absorbing materials *Sound Vib.* **44** 12–7

[5] Koo B, Yi Y, Lee M and Kim B 2017 Effect of particle size and forming pressure on pore properties of Fe-Cr-Al porous metal by pressureless sintering *Met. Mater.* **23** 336–40

[6] Otaru A J, Morvan H P and Kennedy A R 2019 Airflow measurement across negatively-infiltration processed porous aluminium structures *American Institute of Chemical Engineers AIChE J* **65** 1355–64

[7] Jung J H, Krstic V D and Cho H K 2001 Numerical analysis of effective thermal conductivity associated with microstructural changes of porous SiC as an inert-matrix *Met. Mater.* **7** 21–6

[8] Oun H and Kennedy A R 2014 Experimental investigation of pressure drop characterization across multilayer porous metal *Structure, J. Porous Mater* **21** 1133–41

[9] Otaru A J and Kennedy A R 2016 The permeability of virtual macroporous structures generated by sphere-packing models: comparison with analytical models *Scr. Mater.* **124** 30–3

[10] Siddiq A R and Kennedy A R 2017 A novel method for the manufacture of porous structures with Multi-component *coated pores, Materials Letters* **196** 324–7

[11] Langston P and Kennedy A R 2014 Discrete element modelling of the packing of spheres and its application to the structure of porous metals made by infiltration of packed beds of NaCl beads *Powder Technol.* **268** 210–8

[12] Kennedy A R 2012 Porous metals and metal foams made from powders *Powder Metall.* **2** 31–48

[13] Lu T J F and He D 2000 Sound absorption of cellular metals with semi-open cells *J. Acoust. Soc. Am.* **108** 1697–708

[14] Otaru A J 2019 Review on processing and fluid transport in porous metals with a focus on bottleneck structures *Met. Mater. Int.* **26** 510–25

[15] Otaru A J, Morvan H P and Kennedy A R 2019 Numerical modelling of the sound absorption spectra for bottleneck dominated porous metallic structures *Appl. Acoust.* **151** 164–71

[16] Otaru A J, Morvan H P and Kennedy A R 2018 Measurement and simulation of pressure drop across replicated microcellular aluminium in the darcy-forchheimer regime *Acta Mater.* **149** 265–75

[17] Otaru A J, Morvan H P and Kennedy A R 2018b Modelling and optimisation of sound absorption in replicated microcellular metals *Scr. Mater.* **150** 152–5

[18] Lu J J, Hess A and Ashby M F 1999 Sound absorption of metallic foams *America Institute of Physics* **99** 07511–9

[19] Oun H and Kennedy A R 2015 Tailoring the pressure drop in multi-layered open-cell porous inconel structures *J. Porous Mater.* **2** 1627–33

[20] Dukhan N 2013 Principles of Fluid Flow through Open-Cell Metal Foam *Metal Foams: Fundamental and Applications* (United States of America: Inc. Technology and Engineering) pp 1–310

[21] Reutter O, Smirnova E, Sauerhering J, Angel S, Fend T and Pitz-Paal R 2008 Characterization of Air flow through sintered metal foams *ASME J. Fluids Eng.* **130** 051201

[22] Seah K and Sh. Teoh T 1998 Parametric studies of the mechanical behaviour of porous titanium *Met. Mater. Int.* **4** 672–5

[23] Choi Y B, Motoyama T, Matsugi K and Sasaki G 2014 Influence of the specific surface area of a porous nickel to the intermediate compound generated by reaction of a porous nickel & aluminium *Met. Mater. Int.* **20** 741–5

[24] Champoux Y and Stinson M R 1992 On acoustical models for sound propagation in rigid frame porous materials and the influence of shape factors *J. Acoust. Soc. Am.* **92** 1120–31

[25] Ghazi A, Berke P, Ehab Moustafa Kamel K, Sonon B, Tiago C and Massarat T J 2019 Multiscale computational modelling of closed-cell metallic foams with detailed microstructural morphological control *Int. J. Eng. Sci.* **143** 92–114

[26] De Carvalho T P, Morvan H P, Hargreaves D, Oun H and Kennedy A 2017 Pore-scale numerical investigation of pressure drop behaviour across open-cell metal foams *Tran Porous Med.* **117** 311–36

[27] Fand R M, Kim B Y K, Lam A C C and Phan R T 1987 Resistance to the flow of fluids through simple and complex porous media whose matrices are composed of randomly packed spheres *Trans. ASME* **109** 268–73

[28] Kececioglu I and Jiang Y 1994 Flow through porous media of packed spheres saturated with *Water, Transactions of ASME* **116** 164–70

[29] Lage J L, Krueger P S and Narasimham A 2005 Protocol for measuring permeability and form coefficient of porous media *Phys. Fluids* **17** 088101

[30] Otaru A J and Kennedy A R 2019 Investigation of the pressure drop across packed beds of spherical beads: comparison of empirical models with pore-level computational fluid dynamics simulations *ASME Fluids Eng.* **141** 071305

[31] Ergun S and Orning A A 1949 Fluid flow through packed randomly packed columns and fluidized beds *Industrial Engineering Chemistry* **41** 1179–84

[32] Otaru A J 2020 The permeability of replicated microcellular structures in the darcy regime *American Institute of Chemical Engineers AIChE J* **66** e16915

[33] Evans E V 1994 Dynamic measurements of sand Pack thickness and evaluation of non-darcy flow through gravel packs *PhD Dissertation* University of Oklahoma

[34] Chaveteau G 1965 Essai sur la loi de darcy *Doctoral thesis* University of Tolouse

[35] Lage J L, Anthone V B and Nield D A 1997 Two types of non-linear pressure drop versus flow rate relation observed for saturated porous media *J. Fluids Eng.* **119** 700–6

[36] Missbach A 1937 *Listy Cukrovar* 55 (Prague, Czechoslovakia: Technical Information Center, U.S. Army Engineer Waterways Experiments Station, P.O. Box 631, Vicksburg, MS 39180-0631) p 293

[37] Izbash S V 1931 O Filtracii Kropnozernstom Materiale *[Groundwater Flow in the Material Kropnosernstorm?]* (Leningrad, USSR, Russia: Izv. Nauch-noissled, Inst. Gidrotechniki (NIIG))

[38] Ergun S 1952 Fluid flow through packed column *Chem. Eng.* **48** 89–94

[39] Edouard D, Lacroix M, Pham C, Mbodji M and Pham-Huu C 2008 Experimental measurements and multiphase flow models in solid SiC foam beds *AlChE J.* **54** 2823–32

[40] Della Torre A, Montenegro G, Tabor G R and Wears M L 2014 CFD characterization of flow regimes inside open cell foam substrates *Int. J. Heat Fluid Flow* **50** 72–82

[41] Masuoka T and Yakatsu Y 1996 Turbulence model for flow through porous media *Int. J. Heat Mass Transfer* **39** 2803

[42] Otaru A J, Abdulkadir M, Corfield M R, Kenfack A and Tanko N 2020 Computational evaluation of effective transport properties of differential microcellular structures *American Institute of Chemical Engineers AIChE J* (https://aiche.onlinelibrary.wiley.com/doi/abs/10.1002/aic.16928)

[43] Ashby M F, Evans A and Kennedy A R 2006 The Role of oxidation during compaction on the expansion and stability of Al foams made via a PM route *Adv. Eng. Mater.* **8** 568–70

[44] Atwater M A, Guevara L N, Darling K A and Tschopp M A 2018 Solid state porous metal production: A review of the capabilities, characteristics, and challenges *Adv. Eng. Mater.* **20** 1700766

[45] Lefebvre L-P, Banhart J and Dunand D C 2008 Porous metals and metallic foams: current status and recent developments *Adv. Eng. Mater.* **10** 775–87

[46] Lu T J, Stone H A and Ashby M F 1998 Heat transfer in open-cell metal foams *Acta Mater.* **46** 3619–35

[47] Asholt P 1999 *Metal Foams and Porous Metal Structures* ed J Banhart, M F Ashby and N A Fleck (Bremen, Germany: MIT-Verlag) p 133 (http://aluminiumschaum.de/metfoam1999-articles/einzelartikel/metfoam1999-frontmatter-TOC.pdf)

[48] Thomson W 1887 On the Division of Space with Minimum Partitional Area *Philosofical Magazine* **5** 503–14

[49] Weaire D and Phelan R 1994 A counter-example to Kelvin's conjecture on minimal *Surfaces, Philosofical Magazines Letters* **69** 107–10

[50] Gibson L J and Ashby M F 2001 Cellular solids *Structure & Properties* 2 (Cambridge: Cambridge University Press) (https://doi.org/10.1002/adv.1989.060090207)

[51] Du Plessis P, Montillet A and Comiti J 1994 Pressure-drop prediction for flow through high porosity metallic foams *Chem. Eng. Sci.* **49** 3545–53

[52] Bracconi M, Ambrosetti M, Maestri M, Groppi G and Tronconi E 2017 A Systematic procedure for the virtual reconstruction of open-cell foams *Chem. Eng. J.* **315** 608–20

[53] Zielinski T G 2015 Generation of random microstructures and prediction of sound velocity and absorption for open foams with spherical pores *Journal of Acoustical Society of America* **137** 1790–801

[54] Wehinger G D, Heitmann H and Kraume M 2016 An Artificial structure modeler for 3D CFD simulation of catalytic foams *Chem. Eng. J.* **284** 543–56

[55] Rhodes M B 1980 Cellular & non-cellular polyurethanes *Int. Conf. (Strasbourg, France)* pp 803–19

[56] Richardson M and Nandra D 1986 *Cell, Polym.* **5** p423

[57] Montming M D, Tannenbaum A R and Macosko C W 2004 The 3D structure of real polymer foam *Journal of Colloid & Interface Science* **280** 202–423

[58] Watson I G, Lee P D, Dashwood R J and Young P 2006 Simulation of the mechanical properties of an aluminium matrix composite using x-ray micro-tomography *Metal Mater. Trans.* **37A** 551–8

[59] Fularia D, Lee P D and Bernard D 2007 Determining the fluid flow & deformation behaviour of both simulated & measured columnar-dendritic structures in Al-Cu alloys *5th Decennial Int. Conf. on Solidification Processing (Sheffield, United Kingdom)*

[60] Pak T, Archilha N, Mantovani I F, Moreira A C and Butler I B 2018 The dynamics of nanoparticle-enhanced fluid displacement in porous media—a pore-scale study *Sci. Rep.* **8** 11148

[61] Wang L, Dang Z, Li X and Xia Z 2018 , A multi-scale flow model for production performance analysis in shale gas reservoirs with fractal geometry *Sci. Rep.* **8** 11464

[62] Zhu J and Ma J 2018 Extending a Gray lattice boltzmann model for simulating fluid flow in multiscale Porous media *Sci. Rep.* **8** 5826

[63] Petrasch J, Wyss P, Stampili R and Steinfeld A 2008 Tomography-based multiscale analysis of the 3d geometrical morphology of reticulated porous ceramics *J. Am. Ceram. Soc.* **91** 2659–65

[64] Trofimov A, Mishurova T, Lanzoni L, Radi E, Bruno G and Sevostianov T 2018 Microstructural analysis and mechanical properties of concrete reinforced with polymer short fibres *Int. J. Eng. Sci.* **133** 210–8

[65] Narsilio G A, Buzzi O, Fityus S, Yun T S and Smith D W 2009 Upscaling of navier–stokes equation in porous media: theoretical, numerical & experimental approach *Computers & Geotechnics* **36** 1200–6

[66] Bodla K K, Murthy J Y and Garimella S V 2010 Microtomography-based simulation of transport through open-cell metal foams, ctrc research publication *An International Journal of Computation and Methodology* **58** 527–44

[67] Peng S, Hu Q, Dultz S and Zhang M 2012 Using x-ray computed tomography pore structure characterization for berea sandstone: resolution effect *J. Hydrol.* **472-473** 254–61

[68] Inyat A, Freund H, Zeiser T and Schwieger W 2011 Determining the Specific surface area of ceramic foams: the tetrakaidecahedra model revisited *Chem. Eng. Sci.* **66** 1179–88

[69] Dietrich B, Schabel W, Kind M and Martin H 2009 Pressure drop measurements of ceramic sponges—determining the hydraulic diameter *Chemical Engineering Sciences* **64** 3633–40

[70] Wilson D K 1993 Relaxation-matched modelling of propagation through porous media, including fractal pore structure *J. Acoust. Soc. Am.* **94** 1136–45

[71] Menter F and Esch T 2001 Elements of industrial heat transfer predictions, in 16th brazilian congr *Mech. Eng.* 26–30

[72] Darcy H P G 1856 The public fountain of the city of dijon, bookseller of the imperial corps of bridge *Highways and Mines, Quays of Augustins* 49

[73] Dye A L, McClure J E, Miller C T and Gray W G 2013 Description of non-darcy flows in porous medium systems *Phys. Rev. E* **87** 033012

[74] Della Torre A, Lucci F, Montenegro G, Onorati A, Dimopoulus Eggenschwiler P, Tronconi E and Groppi G 2016 CFD modelling of catalytic reactions in open-cell foam substrates *Computer and Chemical Engineering* **92** 55–63

[75] Schneider R, Schindler F and Weiler F 1996b Octree-based generation of hexahedral element meshes *Proc. 5th Int. Meshing Roundtable* (Sandia National Laboratories) pp 205–16

[76] Chen L 2014 *A simple construction of a fortin-operator for the two-dimensional taylor-hood element. department of mathematics* (United States of America: University of California) (https://www.sciencedirect.com/science/article/pii/S0898122114004519)

[77] Simpleware Ltd Reference Guide 2014 Converting 3D images into models Version 7.0

[78] Calmidi V V and Mahajan R L 1999 The effective thermal conductivity of high porosity fibrous metal foams *ASME Journal of Heat Transfer* **121** 466–71

[79] Bonnet J P, Topin F and Tadrist L 2008 Flow laws in metal foams: compressibility and pore size effects *Trans. Porous Med.* **73** 149–63

[80] Gatski T B 2004 Constitutive equations for turbulent flows *Theor. Comput. Fluid Dyn.* **18** 345–69
[81] Yakhot V, Orsag S, Thamgam S, Gatski T and Speziale C 1992 Development of turbulence models for shear flows by a double expansion technique *Physics of Fluids: A* **4** 1510–20
[82] Skjetne W and Auriault J L 1999 High-velocity laminar and turbulent flow in porous media *Transp. Porous Media* **36** 131
[83] Nield D A and Bejan A 1992 *Convection in Porous Media* 2nd ed. (New York: Springer) pp 10–4
[84] Xu W and Jiao Y 2019 Theoretical framework for percolation threshold, tortuosity and transport properties of Porous materials containing 3D non-spherical pores *Int. J. Eng. Sci.* **134** 31–6
[85] Cieszko M 2019 Macroporous Description of Quasi-Static and Quasi-Stationary Processes in Unsaturated Porous Materials *Int. J. Eng. Sci.* **140** 1–16
[86] Bear J 1972 *Dynamics of Fluids in Porous Media.* (New York: Dover Publications, Inc.) pp 124–30
[87] Dybbs A and Edwards R V 1984 A new look at porous media fluid mechanics-darcy to turbulent *in J. Bear, M.Y. Nato ASI series E.* **82** 6175-3
[88] Boomsma K and Poulikakos D 2002 The Effect of comparison and pore size variations on the liquid flow characteristics in metal foams *ASME J. Fluids Eng.* **124** 263–73
[89] Weber L, Ingram D, Guardia S, Athanasiou-Ioannou A and Mortensen A 2017 Fluid flow through replicated microcellular materials in the darcy-forchheimer regime *Acta Mater.* **126** 280–93
[90] Otaru A J 2018 Fluid flow and acoustic absorption in porous metallic structures using numerical simulation and experimentation *PhD Thesis* (United Kingdom: The University of Nottingham)
[91] Mancin S, Zilio C, Diani A and Rossetto L 2013 Air forced convection through metal foams: experimental results & modelling *Int. J. Heat Mass Transfer* **62** 112–23
[92] Phanikumar M S and Mahajan R L 2002 Non-darcy natural convection in high porosity metal foams *International Journal of Heat & Mass Transfer* **45** 3781–93
[93] Bhattacharya A, Calmidi V V and Mahajan R L 2002 Thermophysical properties of high porosity metal foams *Int. J. Heat Mass Transfer* **45** 1017–31
[94] Edouard D, Lacroix M, Huu C P and Luck F 2008 Pressure drop modelling on solid foam: state-of-the-art correlation *Chem. Eng. J.* **144** 299–311
[95] Calmidi V and Mahajan R 2000 Forced convection in high porosity metal foams *ASME J. Heat Transfer* **122** 557–65
[96] Kamath P M, Balaji C and Venkateshan S P 2011 Experimental investigation of flow assisted mixed convection in high porosity foams in vertical channels *International Journal of Heat & Mass Transfer* **54** 5231–41